Supplementary Information

The critical role of configurational flexibility in facilitating reversible reactive metal deposition from borohydride solutions

Nathan T. Hahn,[a,b] Julian Self,[a,c,d] Trevor J. Seguin,[a,c] Darren M. Driscoll,[a,e] Mark A. Rodriguez,[b] Mahalingam Balasubramanian,[a,e] Kristin A. Persson,[a,c,d] Kevin R. Zavadil*[a,b]

[a] Joint Center for Energy Storage Research, Lemont, IL 60439, USA

[b] Material, Physical and Chemical Sciences Center, Sandia National Laboratories, Albuquerque, NM 87185, USA. *Email: krzavad@sandia.gov

[c] Energy Technologies Division, Lawrence Berkeley National Laboratory, Berkeley, CA 94720, USA

[d] Department of Materials Science, University of California Berkeley, Berkeley, CA 94720, USA

[e] Advanced Photon Source, Argonne National Laboratory, Lemont, IL 60439, USA.

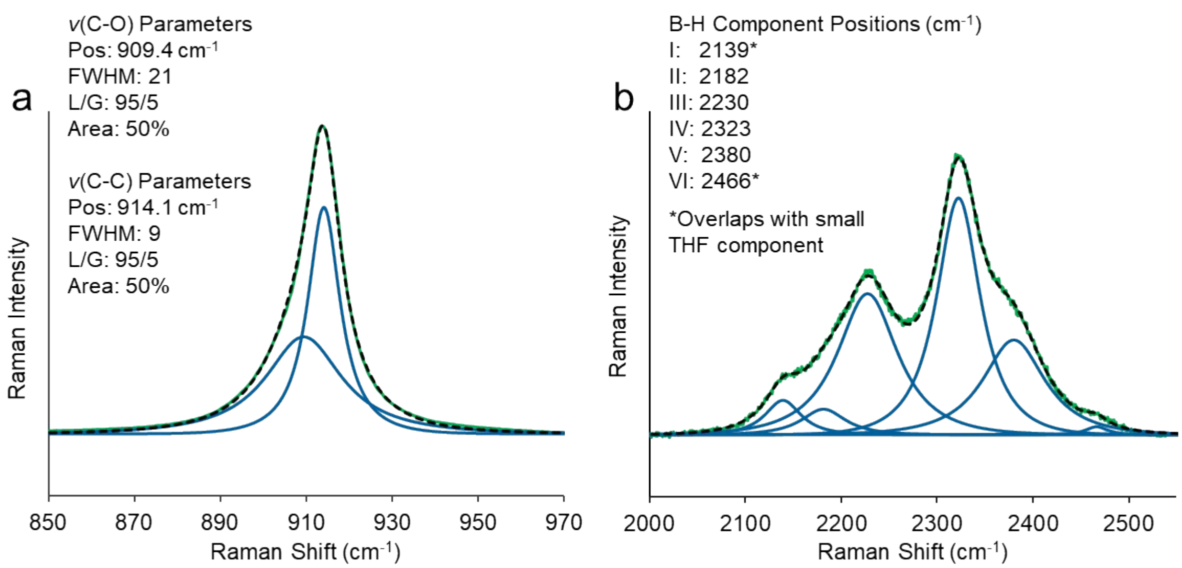

Figure S1. a) Raman spectrum of the *ν*(C-O)/*ν*(C-C) region of neat THF highlighting the two primary vibrational modes in the absence of coordination. b) Raman spectrum of the *ν*(B-H) region highlighting the BH_4^- vibrational modes present in 1.65M $Ca(BH_2)_2$/THF. The spectrum was fit with the minimal number of Lorentzian/Gaussian components (6) required to match the observable points of inflection. In both (a) and (b), the green trace represents the experimental data while the black dashed line shows the sum of the fitted components.

Computational Methods

Molecular Dynamics

To investigate the dielectric increment per salt cluster species, MD simulations were undertaken with 1 given species in a box of 112 THF solvent molecules. Forcefield parameters were taken from Calemen et al. for THF,[1] while the Ca^{2+} parameters used are standard in the OPLS forcefield[2] and BH_4^- parameters are those used by Rajput et al..[3] To equilibrate the simulations before the production runs, steepest descent minimization, isobaric-isothermal equilibration with the Berendsen barostat,[4] and a set of heating and quenching steps were carried out, following the procedures undertaken by Rajput et al.[3] Production runs, undertaken in the canonical ensemble with the velocity rescaling thermostat.[5]

Quantum Chemistry Calculations

Thermal corrections for all free energies were computed under the Quasi-RRHO method of Grimme.[6] In order to account for the solvation environment of chemical moieties, the IEFPCM continuum solvation model was used with a dielectric constant of 7.4, that of neat THF. Formation free energies, ΔG_f, of solvated calcium borohydride complexes containing x BH_4^- and y THF ligands bound to Ca^{2+} were computed from the following equation, where G(X) is the computed free energy of species X:

$$\Delta G_f = G([Ca(BH_4)_x THF_y]_{2-x}]) - G(Ca^{2+}) - xG(BH_4^-) - yG(THF)$$

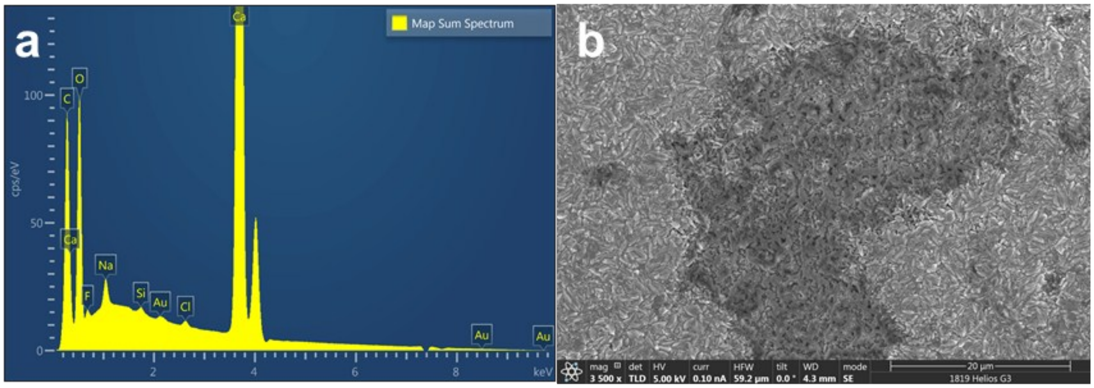

Figure S2. Energy dispersive x-ray spectrum (a) and corresponding scanning electron microscopic image (b) of a 2 micron thick Ca deposit on Au generated at 4 mA/cm^2 in 1.65 M $Ca(BH_4)_2$/THF confirming composition as primarily Ca. The C and O content observed are likely byproducts of the remnant parasitic reaction with the electrolyte (97% CE) or residual oxidants in the glove box or during sample transfer to SEM vacuum. This transfer into vacuum is conducted in a well-purged glove bag under flowing UHP Ar.

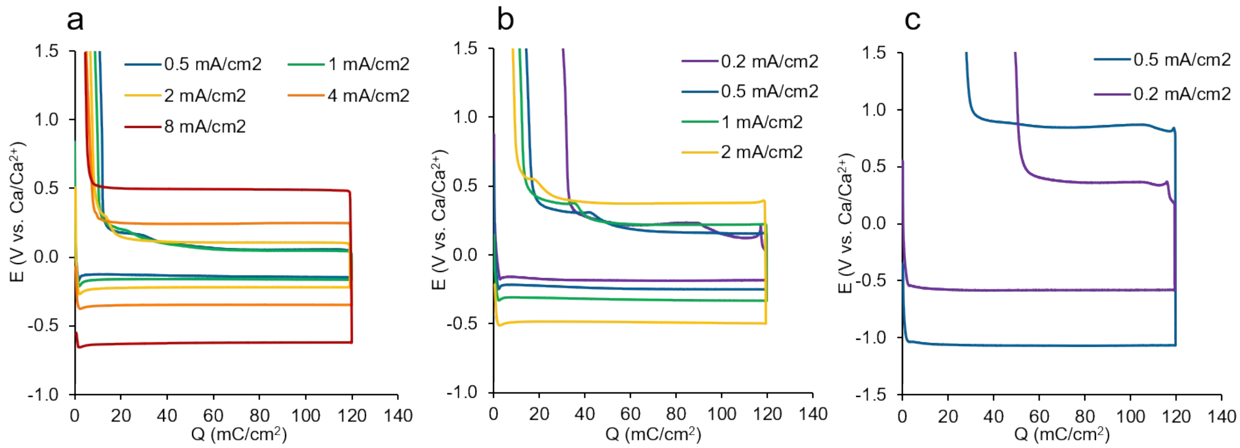

Figure S3. Chronopotentiograms (CP) depicting the constant current deposition/dissolution of Ca^0 from a Au substrate across several current densities and $Ca(BH_4)_2$ concentrations in THF: a) 1.65 M, b) 0.85 M, c) 0.43 M. A 1.5 V cut-off was used for the anodic polarization steps in order to avoid BH_4^- oxidation, which begins > 2 V vs. Ca/Ca^{2+}.

Comparative $Ca(BH_4)_2$ and $Mg(BH_4)_2$ Cyclic Voltammetric Responses in THF

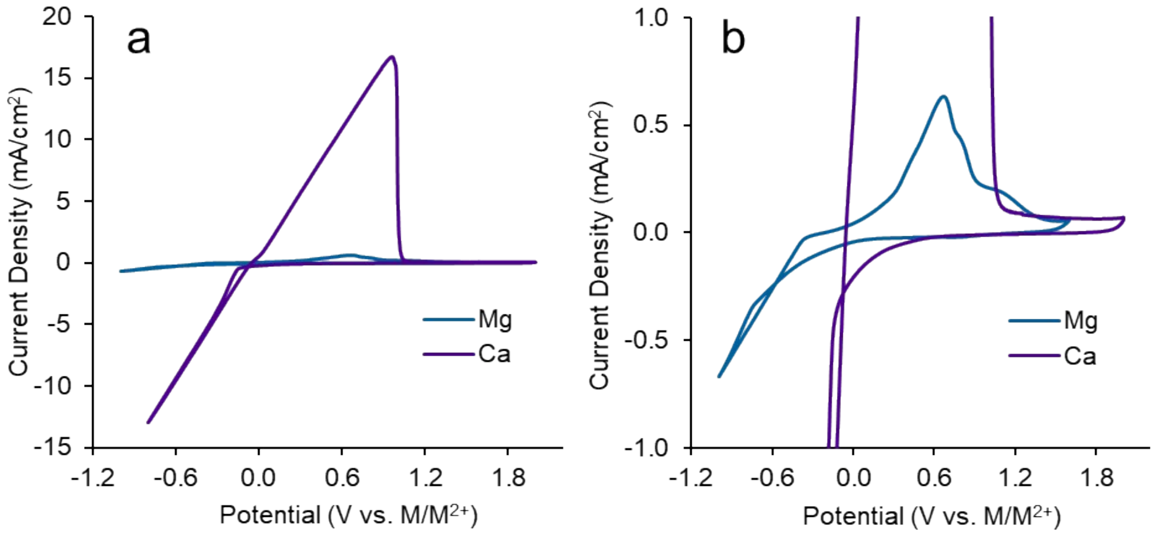

Figure S4. a) Cyclic voltammograms of reversible metal deposition in saturated $Mg(BH_4)_2$ and $Ca(BH_4)_2$ electrolytes in THF on Au working electrodes (scan rate = 50 mV/s). Measured coulombic efficiencies are 74% and 97%, respectively. b) The same voltammograms as shown in (a) but with a magnified current scale highlighting $Mg(BH_4)_2$ deposition/dissolution behavior.

The data of Figure S4 highlight the differences in voltammetric response of saturated $Mg(BH_4)_2$/THF (ca. 1M) and $Ca(BH_4)_2$/THF (1.65 M). Use of the Mg salt increases the metal deposition overpotential by ca. 500 mV, reduces the rate of deposition by > 20X at equivalent potential, and decreases the Coulombic efficiency relative to the Ca salt (74 vs. 97%). The origin of the current distribution in the Mg stripping curve is unknown but is likely related to a larger fraction of parasitic decomposition of the electrolyte (lower CE) at the greater overpotential (ca. 500 mV vs. Ca) required for Mg deposition. Limited Mg alloying with the Au substrate may also play a role in shifting anodic current to more positive potential during stripping. We note that repeated CV cycles on the same electrode were essentially invariant with cycle number over the limited durations tested for both salts, indicating that passivation was not significant for either Ca or Mg.

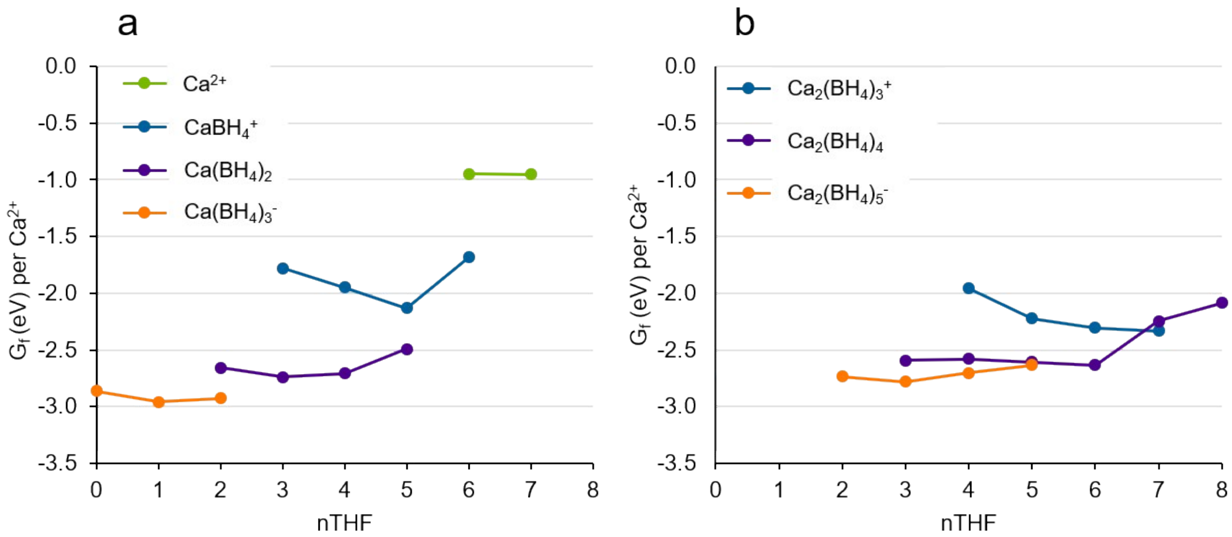

Figure S5. DFT-calculated free energies of formation (referenced to $THF_3Ca(BH_4)_2$) for various Ca^{2+} complexes as a function of total THF:Ca^{2+} CN for monomers (a) and dimers (b).

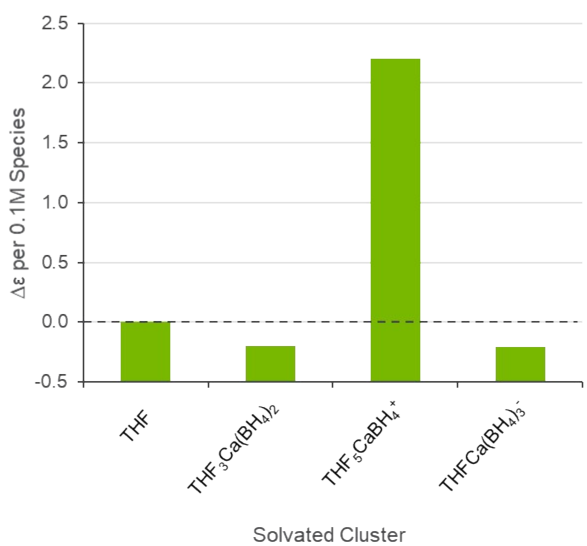

Figure S6. Calculation of the change in solution permittivity predicted based on the formation of 0.1 M of various calculated electrolyte clusters.

$THF_6Ca_2(BH_4)_4$ $THF_7Ca_2(BH_4)_4$ $THF_8Ca_2(BH_4)_4$

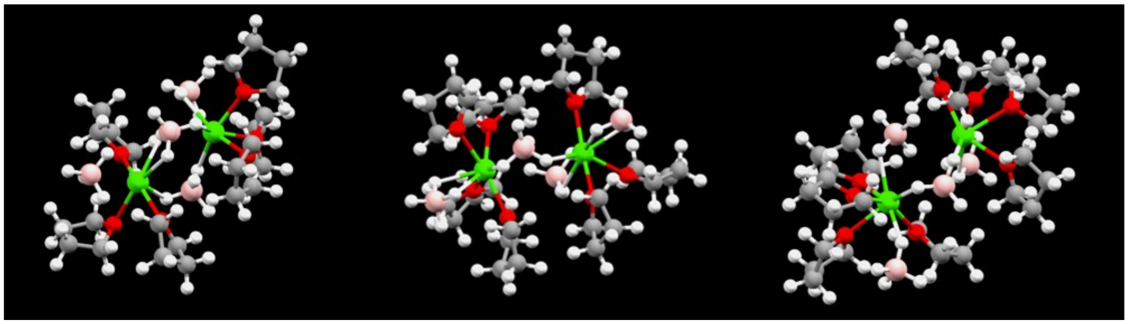

Figure S7. A set of $THF_xCa_2(BH_4)_4$ dimer structures optimized by DFT free energy minimization for x = 6, 7, and 8, yielding Ca-Ca distances of 4.22, 4.56, and 4.40 Å, respectively, consistent with the apparent Ca-Ca correlation distance (4.44 Å) observed in the $Ca(BH_4)_2$/THF EXAFS.

Discussion of X-ray Absorption Spectroscopy Approach and Results

X-ray absorption spectroscopy was performed to understand the local coordination environment around the Ca^{2+} ions in solution. Studies were performed in transmission mode for the 1.5 M $Ca(BH_4)_2$ sample and performed in fluorescence mode, using an energy dispersive, multi-element fluorescence detector (Vortex-ME4), for the 0.2 M $Ca(BHFIP)_2$ sample. Ionization gas chambers before and after the sample were used to measure X-ray absorption for transmission mode experiments. The inert gas composition of the ion chambers was 20% N_2, 80% He and 100% N_2 for I_o (before the sample) and I_t (after the sample), respectively. Each sample was attached to a vertical manipulator within a He-purged chamber. Fluorescence detection utilized a dead-time correction to account for saturation effects and the total count rate did not exceed 80000 counts per element at the white line. The beam was focused into a 2 mm by 0.5 mm beam size and detuned 15% with the harmonic cut-off set to 6 keV. All samples were energy aligned with regards to a Ti foil and normalized using the Athena software program. At the Ca K-edge, mutli-electron transitions appear in the EXAFS region at roughly 2.7, 3.1 and 10.3 $Å^{-1}$.[11-12] The 10.3 $Å^{-1}$ multi-electron excitation (MEE) was accounted for using an arctangent correction function.[13] The other two MEEs have little effect on the regions of interest within the Fourier transformed data and were otherwise ignored.

Model Ca^{2+} photoelectron pathways through THF, BH_4 and coordinated Ca atoms were generated with the help of FEFF 6.0. These pathways included Ca–O and Ca–C single scattering and Ca–O–C and Ca–O–Ca–O (rattle between the same oxygen) multiple scattering from THF, as schematically depicted in Figure S8. Additionally, a Ca–B pathway from BH_4 and a Ca–Ca pathway associated with potential dimer configurations were studied. Model paths originating from Ca-H_{BH4} were not included in the overall fit. This is because the Ca-H-B angle as predicted by DFT was far from 180° and not expected to contribute to the overall EXAFS spectrum.

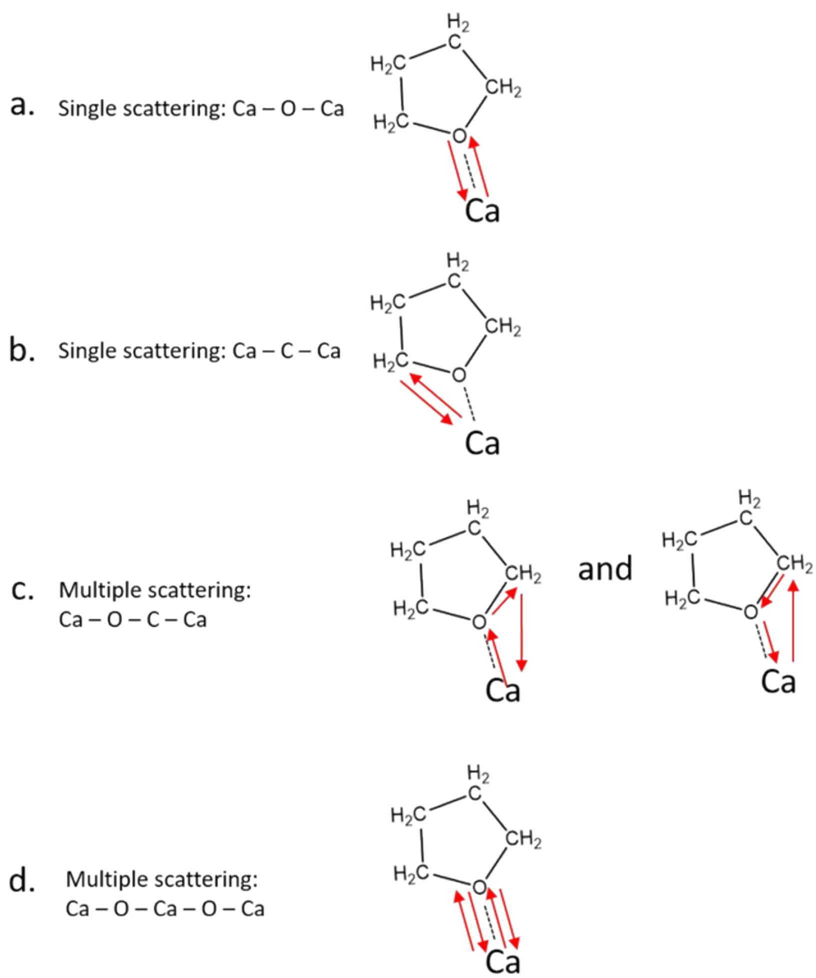

Figure S8. Schematic representation of the photoelectron paths used to model the Ca–THF contributions to the EXAFS.

Upon calculation of an individual scattering pathway, each path was allowed four variables including the coordination number (CN), inner potential shift (ΔE_0), adjustment of the half path length (ΔR_0) and Debye-Waller factor (σ^2). Total coordination around a single Ca^{2+} cation was set equal to 8 while the coordination number of Ca-O and Ca-B were allowed to float in relation to the total coordination. This was done in order to keep the number of independent variables well below the information content available in the EXAFS data. The many-body amplitude reduction factor (S_0^2) was set equal to 0.95 which is consistent with previous literature.[11] A single ΔE_o was found sufficient for all paths. The data was k windowed between 3

Structural Parameter	Fitted EXAFS Model	DFT $THF_8Ca_2(BH_4)_4$ Model
*CN: Ca–O_{THF}	6.3 ± 0.9	4.0
%CN: Ca–B	1.7 ± 0.9	2.5
ΔE_0	0.5 ± 1.9 eV	-
Ca–O_{THF}	2.41 ± 0.02 Å	2.45 Å
$\sigma^2_{O, THF}$	0.015 ± 0.002 Å^2	-
$\sigma^2_{C, THF}$	0.022 ± 0.007 Å^2	-
$\sigma^2_{OC, THF}$	0.012 ± 0.005 Å^2	-
$\sigma^2_{OO, THF}$	#0.06 ± 0.02 Å^2	-
Ca–B	3.11 ± 0.15 Å	3.01 Å
σ^2_{B}	0.014 ± 0.014 Å^2	-
Ca–Ca_{Dimer}	4.44 ± 0.05 Å	4.40 Å
$\sigma^2_{Ca, Dimer}$	0.013 ± 0.011 Å^2	-
*Total Coordination # fixed to 8 %Ca–Ca coordination # fixed to ½ of the CN of Ca–B #The Ca–O–Ca–O rattle path is computed to be 4x the Ca–O path		

Table S1. Fitted EXAFS parameters for the 1.5 M $Ca(BH_4)_2$ /THF electrolyte and comparison with an exemplar DFT structural model as seen Figure S7.

– 11.8 Å^{-1} and fitted between 1.60 – 4.37 Å. The corresponding fit to the real part of the FT, which has both amplitude and phase information, is presented in Figure 3c of the main text with the parameter fit results displayed in Table S1. Additionally, the specific contributions associated with Ca–B and Ca–Ca pathways are plotted against the experimental data in Figure S9. From this comparison, we note the dimer induced Ca–Ca scattering pathway aligns with the 4 Å feature in the experimental data as mentioned in the previous paragraph.

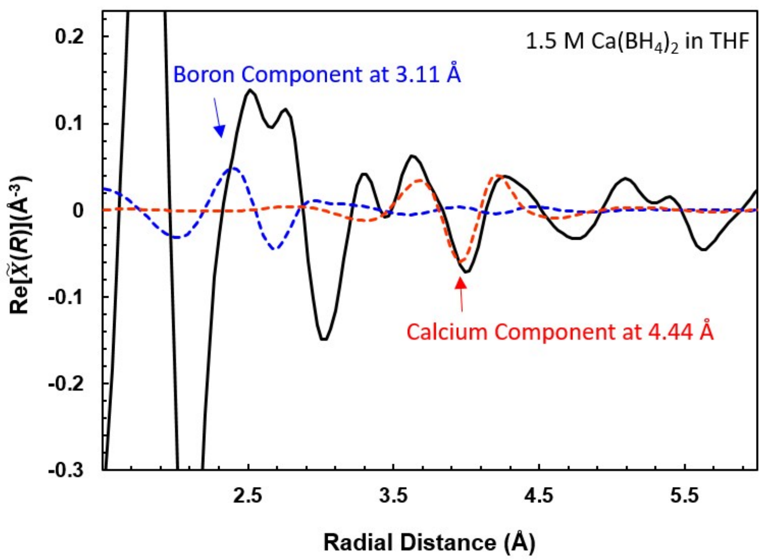

Figure S9. k^2-weighted Re[$\tilde{\chi}(R)$] for the Ca K-edge of $Ca(BH_4)_2$ (black trace) and the components for the Ca–B (blue trace) and Ca–Ca (red trace). Each component is calculated through FEFF 6.0 and fitted to the experimental data.

To validate the addition of a Ca–Ca dimer and a Ca–B single scattering pathway, each path was systematically removed from the fitting procedure. A comparison between the full fit and the fit without a specific component can be used to study the effect that each path has on the statistical rigor of the overall fit. Upon removal of the Ca–Ca dimer path, the model fit of the high r-space data was greatly reduced and is reflected in both the reduced-χ^2 (χ_ν^2) and R factor as shown in Table S2. The almost 50% improvement in the χ_ν^2, which considers the number of floating variables used in each fit, is convincing evidence of the presence of Ca dimers within the 1.5M $Ca(BH_4)_2$ salt solution. This result further validates the existence of

Ca–BH_4 ion pairs in the first coordination shell as the presence of Ca-Ca dimers without one or more BH_4 units bridging the two dications is highly unlikely, as demonstrated by DFT.

	χ_ν^2	R-factor
Full Fit	51.7	0.0092
Fit Removing Ca Path	92.1	0.019

Table S2. Fit statistics including and excluding the Ca–Ca dimer path

Crystal Structure Refinement Details

The $Ca(BH_4)_2$/THF crystal structure was solved using Direct Methods which resulted in determination of all non-H atoms in the structure. Anisotropic atomic displacement parameters were refined for all non-H atoms in the structure (i.e. Ca, O, B, C). Subsequent refinements revealed Q peaks associated with bound H atoms. H atoms for the THF molecules were predicted and refined using the Riding model and the H-C distances were restrained. An isotropic atomic displacement parameter (U_{iso}) for H on the THF molecules was restrained to 1.2 times the U_{iso} of the respective coordinated C atom to which they were bound. In contrast, the H atoms that made up the borohydride tetrahedra were not as easily determined and refined to stable locations about the B atom based on the X-ray Diffraction data alone. Instead, H positions were estimated in terms of location using observed Q peaks near the B atoms during refinement cycles of the X-ray Diffraction data, and then subsequently modeled via energy minimization via Density Functional Theory (DFT) models. These modeled locations for the H atoms on the borohydride molecules were then fed back into the final X-ray structure and restrained in terms of bond distances and angles as dictated by the DFT output. The U_{iso} values of the bound H atoms on the borohydride molecules were restrained to be identical for all eight of the H atoms that were present on the two different borohydride tetrahedra. This was done to stabilize the isotropic atomic displacement parameters of the H atoms. Structure solution of the G1 crystal structure was performed in a similar fashion, but due to the improved resolution of the X-ray data the H atoms on the borohydride molecules could be refined directly without DFT modeling required. The Table S3 documents the crystallographic data for the solvate structures of $Ca(BH_4)_2$ with THF and G1.

Sample	a (Å)	b (Å)	c (Å)	β (°)	V (Å^3)	Formula	Space group	Z	R_p	R_{wp}
$THF_2Ca(BH_4)_2$	4.2819(9)	18.053(4)	8.0685(17)	90.142(9)	623.70	$C_8H_{24}B_2CaO_2$	$P2_1$ (4)	2	8.03	22.34
$G1_2Ca(BH_4)_2$	8.6747(8)	12.5121(10)	14.4578(12)	102.136(4)	1534.16	$C_8H_{28}B_2CaO_4$	$P2_1/c$ (14)	4	4.44	12.01

Table S3. Crystallographic parameters for the solvate structures of $Ca(BH_4)_2$ with THF and G1

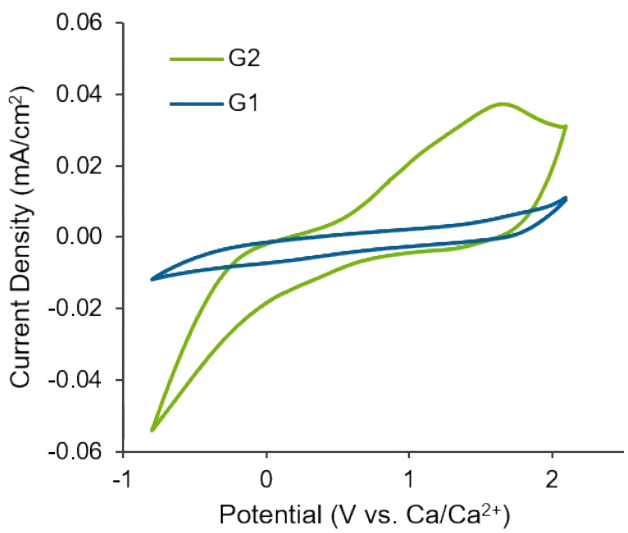

Figure S10. Representative cyclic voltammograms measured for electrolytes containing the $THF_2Ca(BH_4)_2$ salt dissolved at near saturated concentration in G1 (< 25 mM) and G2 (100 mM); scan rate = 25 mV/s. These solutions possess very low ionic conductivity (0.0021 mS/cm and 0.0079 mS/cm, respectively) and exhibit essentially no reversible Ca plating ability, demonstrating the importance of THF in facilitating ionic cluster formation through reconfiguration of multimer intermediates.

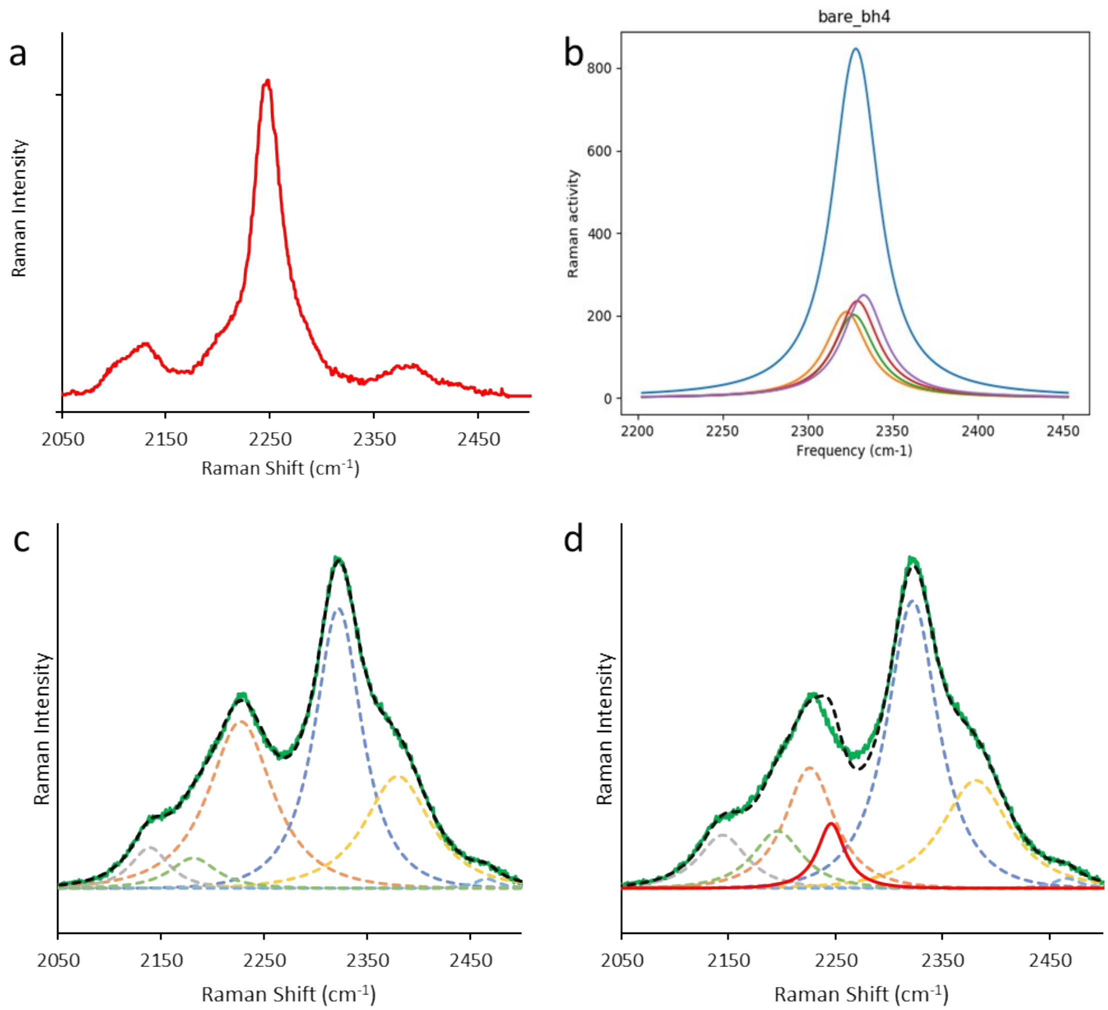

Figure S11. a) Raman *v*(B-H) spectral region measured for a weakly interacting NBu_4BH_4 salt dissolved in THF yielding a dominant narrow band corresponding to a hypothesized free BH_4^- anion. b) Computationally simulated Raman spectrum for free BH_4^- in THF confirming the presence of a narrow composite *v*(B-H) band. The frequency of this band is overestimated with respect to experiment due to neglecting anharmonicity in the calculation. c,d) Experimental spectral band fitting examples in which the primary free BH_4^- band measured in (a) was included (solid red line) in the spectral deconvolution of the 1.65M $Ca(BH_4)_2$/THF solution at a level of 0%

(c) or 5% (d), illustrating the fitting error with free BH_4^- inclusion and arguing its minimal presence in the electrolyte.

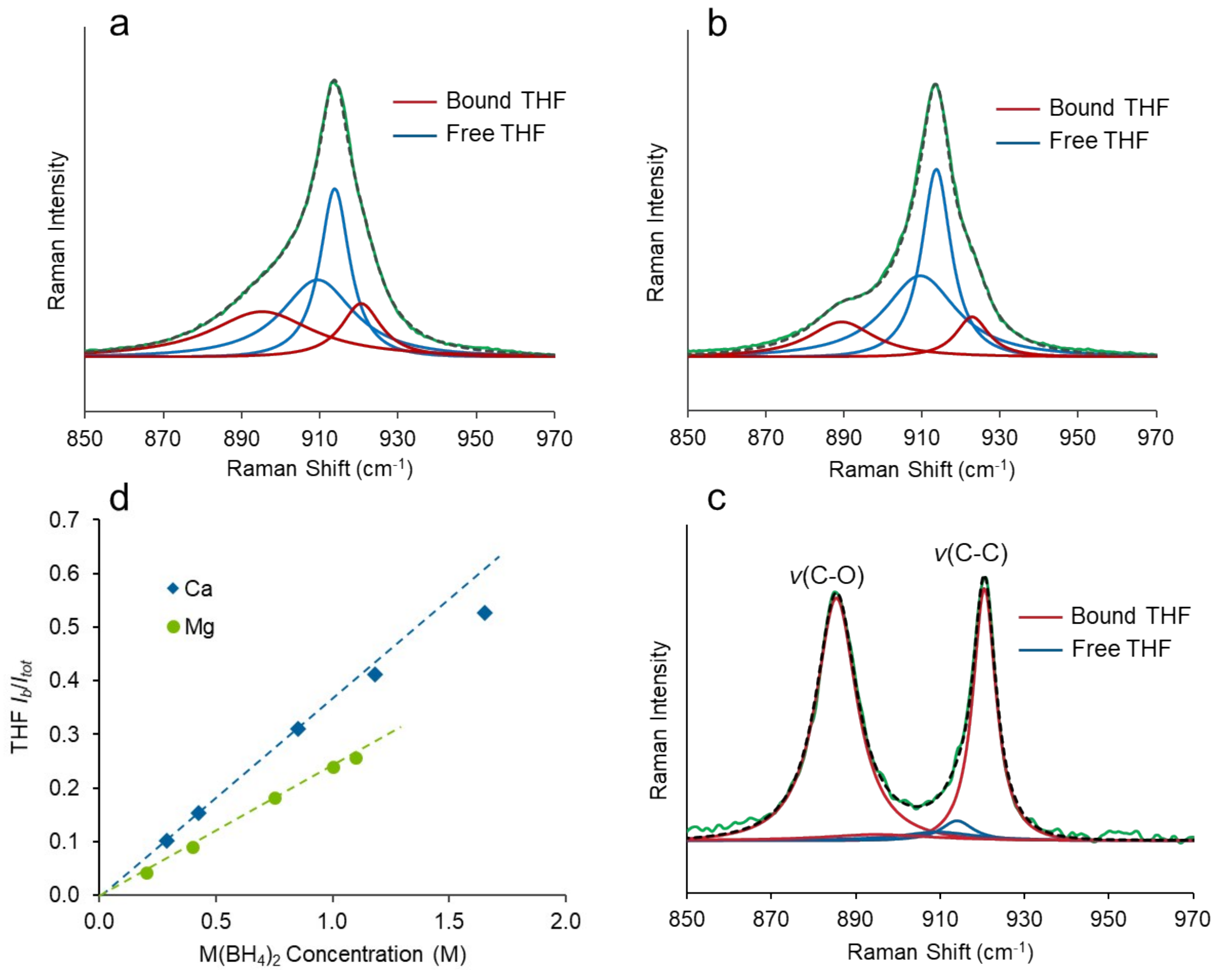

Figure S12. a-c) Raman spectra of the *v*(C-O)/*v*(C-C) region highlighting vibrational modes associated with free (blue) and bound (red) THF molecules. a) 1.2 M $Ca(BH_4)_2$/THF solution. b) 1 M $Mg(BH_4)_2$/THF solution. c) $THF_2Ca(BH_4)_2$ solid. In all cases the green trace represents the experimental data while the black dashed line is the sum of the individual fitted components. d) Ratios of the integrated intensity of bound THF (I_b) to the total integrated intensity of THF within the v(C-O)/v(C-C) region (I_{tot}) as a function of concentration for $Ca(BH_4)_2$ and $Mg(BH_4)_2$. Linear extrapolation of the low concentration trends (dashed lines) reveals two insights: 1) the average THF:Ca^{2+} coordination number (proportional to the slope of this extrapolation) is higher than that of THF:Mg^{2+} at low concentration ; 2) the THF:Ca^{2+} coordination number decreases at high concentrations while the THF:Mg^{2+} coordination number remains constant with concentration.

References

1. Caleman, C.; van Maaren, P. J.; Hong, M.; Hub, J. S.; Costa, L. T.; van der Spoel, D., Force Field Benchmark of Organic Liquids: Density, Enthalpy of Vaporization, Heat Capacities, Surface Tension, Isothermal Compressibility, Volumetric Expansion Coefficient, and Dielectric Constant. *J. Chem. Theory Comput.* **2012,** *8*, 61-74.
2. Jorgensen, W. L.; Maxwell, D. S.; Tirado-Rives, J., Development and Testing of the OPLS All-Atom Force Field on Conformational Energetics and Properties of Organic Liquids. *Journal of the American Chemical Society* **1996,** *118* (45), 11225-11236.
3. Rajput, N. N.; Qu, X.; Sa, N.; Burrell, A. K.; Persson, K. A., The Coupling between Stability and Ion Pair Formation in Magnesium Electrolytes from First-Principles Quantum Mechanics and Classical Molecular Dynamics. *Journal of the American Chemical Society* **2015,** *137* (9), 3411-3420.
4. Berendsen, H. J. C.; Postma, J. P. M.; Gunsteren, W. F. v.; DiNola, A.; Haak, J. R., Molecular dynamics with coupling to an external bath. *The Journal of Chemical Physics* **1984,** *81* (8), 3684-3690.
5. Bussi, G.; Donadio, D.; Parrinello, M., Canonical sampling through velocity rescaling. *The Journal of Chemical Physics* **2007,** *126* (1), 014101.
6. Grimme, S., Supramolecular Binding Thermodynamics by Dispersion-Corrected Density Functional Theory. *Chemistry – A European Journal* **2012,** *18* (32), 9955-9964.
7. Pliego, J. R.; Riveros, J. M., The Cluster−Continuum Model for the Calculation of the Solvation Free Energy of Ionic Species. *The Journal of Physical Chemistry A* **2001,** *105* (30), 7241-7247.
8. Marcus, Y., *Ion Solvation*. John Wiley and Sons Limited: 1986.
9. Trasatti, S., The absolute electrode potential: an explanatory note (Recommendations 1986). *Journal of Electroanalytical Chemistry and Interfacial Electrochemistry* **1986,** *209* (2), 417-428.
10. Rumble, J. R., *CRC Handbook of Chemistry and Physics*. CRC Press/Taylor and Francis: 2018.
11. Fulton, J. L.; Heald, S. M.; Badyal, Y. S.; Simonson, J. M., Understanding the Effects of Concentration on the Solvation Structure of Ca2+ in Aqueous Solution. I: The Perspective on Local Structure from EXAFS and XANES. *The Journal of Physical Chemistry A* **2003,** *107* (23), 4688-4696.
12. Dang, L. X.; Schenter, G. K.; Glezakou, V.-A.; Fulton, J. L., Molecular Simulation Analysis and X-ray Absorption Measurement of Ca2+, K+ and Cl- Ions in Solution. *The Journal of Physical Chemistry B* **2006,** *110* (47), 23644-23654.
13. Ravel, B.; Newville, M., ATHENA, ARTEMIS, HEPHAESTUS: data analysis for X-ray absorption spectroscopy using IFEFFIT. *Journal of Synchrotron Radiation* **2005,** *12* (4), 537-541.